



# The FALCON double-detector Laue diffractometer add-on for grain mapping at POLDI

Stavros Samothrakitis,<sup>a,\*</sup> Camilla Buhl Larsen,<sup>a</sup> Anders Kaestner,<sup>a</sup> Efthymios Polatidis,<sup>a</sup> Jan Čapek,<sup>a</sup> Jan Hovind,<sup>a</sup> Andrin Fazan,<sup>a</sup> John Allibon,<sup>b</sup> Matteo Busi,<sup>a</sup> Søren Schmidt,<sup>c</sup> Jaromír Kopeček<sup>d</sup> and Markus Strobl<sup>a,e</sup>

Received 23 June 2023

Accepted 4 November 2023

Edited by G. J. McIntyre, Australian Nuclear Science and Technology Organisation, Lucas Heights, Australia

**Keywords:** Laue 3D neutron diffraction tomography; three-dimensional grain mapping; neutron detector optimization; neutron diffraction imaging; POLDI; pulse-overlap diffractometer; FALCON; fast-acquisition Laue camera for neutrons.

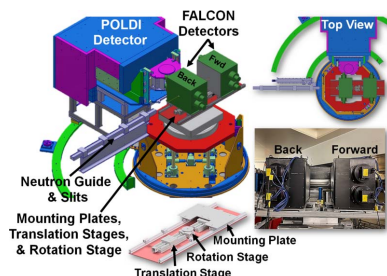
<sup>a</sup>Applied Materials Group, Laboratory for Neutron Scattering and Imaging, Paul Scherrer Institut, Forschungsstrasse 111, CH-5232 Villigen PSI, Switzerland, <sup>b</sup>Institut Laue–Langevin, 71 avenue des Martyrs CS 20156, 38042 Grenoble Cedex 9, France, <sup>c</sup>European Spallation Source ERIC, PO Box 176, Lund 22100, Sweden, <sup>d</sup>FZU Institute of Physics, Czech Academy of Sciences, Na Slovance 1992/2, 1822 Prague, Czech Republic, and <sup>e</sup>Niels Bohr Institute, University of Copenhagen, Blegdamsvej 17, 2100 Copenhagen, Denmark. \*Correspondence e-mail: stavros.samothrakitis@psi.ch

Laue 3D neutron diffraction tomography (Laue 3DNDT) is a novel tomographic approach that enables non-destructive resolution of the 3D microstructure of polycrystalline materials, utilizing a high-intensity white beam of neutrons, resulting in high experimental efficiency. This article describes the functionality of the fast-acquisition Laue camera for neutrons (FALCON), a double-detector system setup used for Laue 3DNDT experiments at the pulse-overlap diffractometer (POLDI) at the SINQ neutron source of the Paul Scherrer Institute. The reported commissioning includes standard experimental protocols, strategies for acquiring data and a detailed characterization of the measurement system. Finally, single-crystal measurements for calibration and a full grain map of a CoNiGa oligocrystalline sample, extracted from a pilot study, are presented. A detailed understanding of the performance of the FALCON instrumentation is vital for the future advancement of the Laue 3DNDT algorithm, including, but not limited to, improved morphology reconstructions and strain mapping.

## 1. Introduction

By Laue diffraction, we refer to the diffraction method that uses a broad wavelength (white beam) spectrum of neutrons or X-rays to examine crystallographic properties. Its primary purpose is to evaluate the quality of single-crystal samples and adjust their orientation before additional scattering experiments. More intricate applications of Laue diffraction include investigations of structural and magnetic phase transitions (Binns *et al.*, 2016; Gorbunov *et al.*, 2018), diffuse scattering measurements (Popov *et al.*, 2015), complex structure refinements (Cooper & Myles, 2000; Zerdane *et al.*, 2015), including fitting of the positions of hydrogen atoms (Novelli *et al.*, 2021), and texture and twinning characterization (Barabash *et al.*, 2015). These all benefit from the fast-acquisition times that one attains using a broad-band wavelength spectrum, with corresponding high flux at the sample, which makes it possible to survey large parts of reciprocal space quickly, even with small samples.

In recent years, we have extended the use of Laue neutron diffraction by developing a novel diffractive tomographic imaging approach, namely Laue 3D neutron diffraction tomography (Laue 3DNDT<sup>1</sup>) (Raventós *et al.*, 2019), which makes it possible to resolve the 3D microstructure of polycrystalline



<sup>1</sup> Laue 3DNDT is an extension of Laue 3DND [as was originally referred to by Raventós *et al.* (2019)] to also include the potential of grain morphology reconstruction.

materials non-destructively. Laue 3DNDT comes as part of an extensive effort to develop 3D characterization methods to investigate, among others, grain-boundary behaviour and interactions, defect formation and propagation, texture evolution, microstructural stability and recrystallization, anisotropic properties and strain evolution, phase transformations and martensitic behaviour, and grain growth. Over the course of the past two decades, the field of materials science and crystallography has witnessed several such innovative approaches for 3D microstructure analysis, using X-rays (Poulsen *et al.*, 2001; Larson *et al.*, 2002; Jensen *et al.*, 2006; Johnson *et al.*, 2008; Ludwig *et al.*, 2008, 2009*a,b*; Lienert *et al.*, 2011; Jensen & Poulsen, 2012; McDonald *et al.*, 2015), electrons (Groeber *et al.*, 2006; Zaefferer *et al.*, 2008; Liu *et al.*, 2011; Konijnenberg *et al.*, 2015; Stechmann *et al.*, 2016; Smeets *et al.*, 2018; Zhu *et al.*, 2022) and neutrons (Peetermans & Lehmann, 2013; Woracek *et al.*, 2014, 2018; Peetermans *et al.*, 2014; Sato *et al.*, 2017; Cereser *et al.*, 2017). X-ray-based methods, such as 3D X-ray diffraction (Poulsen *et al.*, 2001) and laboratory diffraction contrast tomography (McDonald *et al.*, 2015), and electron-based methods, most notably 3D electron backscatter diffraction (3D EBSD) (Groeber *et al.*, 2006), have demonstrated their prowess in offering insight into material structures, and have paved the way for characterizing grain orientations and morphologies in three dimensions at the micro- and nano-scale. However, both come with constraints, either due to limited penetration ability into metallic bulk specimens or due to being destructive. Alternatively, neutron imaging and diffraction techniques, such as cold neutron diffraction contrast tomography (Peetermans *et al.*, 2014) and time-of-flight 3D neutron diffraction in transmission mode (Cereser *et al.*, 2017), have emerged as powerful non-destructive tools for revealing the internal structures and crystallographic information within large coarse-grained metallic samples, complementing X-rays and electrons.

While similar to standard single-crystal Laue diffraction, Laue 3DNDT excels by being able to index data from a polycrystalline sample containing a large number of grains, and resolve grain positions, orientations and morphology without having to resort to a scanning diffraction approach or requiring input from monochromatic measurements. Hence, with Laue 3DNDT, high experimental efficiency is achieved. However, the consequence of using the full neutron spectrum of the beamline is densely spot-populated detector images without wavelength information for each diffraction spot, necessitating careful image processing, data evaluation and indexing through exhaustive Laue pattern fitting (see Section 2.3). As such, to continually enhance its capabilities for addressing multi-grain indexing efficiently, Laue 3DNDT undergoes ongoing development and evolution. In collaboration with the Swiss Data Science Center, a pioneering approach based on an optimal transport framework (Kolouri *et al.*, 2017) is currently under development. This involves solving a convex optimization problem where grain orientations, positions and their assignments to spots are optimized together, while robustly handling outliers. By also integrating machine-learning techniques for image processing and lever-

aging GPU nodes, this approach will not only deliver more robust results but also significantly reduce analysis time. As a result, Laue 3DNDT will be complementary and comparative to other contemporary methodologies such as LaueNN – a neural-network-based approach designed to index diffraction spots in synchrotron X-ray Laue microdiffraction experiments (Purushottam Raj Purohit *et al.*, 2022).

For our experimental work during the development of the Laue 3DNDT method and corresponding dedicated algorithms, we utilized the fast-acquisition Laue camera for neutrons (FALCON) double-detector system, which was built and operated at the E11 beam port of the BER II reactor at Helmholtz-Zentrum Berlin (HZB), Germany (Iles & Schorr, 2014). After operation of BER II ceased, the FALCON detectors were transferred to the Paul Scherrer Institute (PSI) in 2020, where they can be used as an optional add-on setup at the pulse-overlap diffractometer (POLDI) instrument (Stuhr *et al.*, 2006). With the establishment of FALCON at PSI, the Laboratory for Neutron Scattering and Imaging (LNS) expands its suite of instruments for condensed matter physics and materials science studies.

Here, we describe the functionality of the FALCON double-detector system, in conjunction with the Laue 3DNDT method, when used at the POLDI instrument. We include a description of typical experimental procedures and data-acquisition strategies for optimal experimental outcomes. Future method development of the Laue 3DNDT algorithm, including improved morphology reconstruction and strain mapping, is dependent on having detailed knowledge of the detector performance. As such, we carried out comprehensive detector characterization measurements to calculate the resolution of the optical system and to estimate any remnant optical-distortion effects from the built-in camera distortion correction. Additionally, a standard ruby single-crystal calibration sample was measured, at different configurations, for data refinement, as well as for comparative analysis of the FALCON performance between E11 and POLDI. Finally, an oligocrystalline CoNiGa ferromagnetic shape-memory alloy (FSMA) was measured and a full grain map was extracted, as a first indexing example and feasibility study at POLDI.

While our article centres on the FALCON double-detector system and its integration at the POLDI instrument, we recognize the importance of placing this work within the broader context of advanced diffraction and imaging techniques. By acknowledging these parallel methodologies, we underscore the collaborative efforts within the scientific community to enhance our understanding of materials' microstructural features. This acknowledgment serves to align our work with the ongoing advancements and multi-faceted approaches that collectively shape the landscape of modern materials characterization.

## 2. FALCON at POLDI

### 2.1. Technical description

A schematic drawing of the FALCON detectors, along with their mounting system, and the POLDI neutron guide/slit

Table 1

Specification of the FALCON detectors.

|                       |   |
|-----------------------|---|
| Pixel count           | 2000 × 2000 per camera, 4000 × 4000 per quad                    |
| Input pixel size      | 103 µm  |
| Input active area     | 412 × 412 mm per scintillator                                   |
| Scintillator          | <sup>6</sup> LiF/ZnS:Ag, 210 µm thickness, on 1.15 mm aluminium |
| Energy response       | High absorption for thermal neutrons                            |
| Coupling to CCD       | Via coherent straight fibre optic                               |
| CCD pixel size        | 7.4 µm square   |
| Cooling               | Dual-stage Peltier, with secondary air cooling                  |
| Grey-scale resolution | 16 bit  |
| Readout speed         | 12 MHz  |
| Intensifier gain      | User variable via software in 4096 steps, 1000:1 gain range     |
| Binning               | User selectable from 1 × 1 to 8 × 8                             |

system and sample area is given in Fig. 1. FALCON consists of two detectors: one for forward scattering (Fwd) and one for back scattering [see Fig. 1(a)]. The front end of each detector is composed of a large area (412 × 412 mm active area) <sup>6</sup>LiF/ZnS:Ag scintillator with a thickness of 210 µm, providing high neutron-capture efficiency. Four high-performance thermoelectrically cooled image-intensified CCD (iCCD) cameras, with a 4000 × 4000 (h × w) total pixel area (103 µm nominal pixel size) per detector, record the light signal from the scintillator. The cameras view the scintillators via 45° mirrors, avoiding the direct neutron path. Both detectors additionally feature a central hole with a diameter of 20 mm, allowing the direct beam to pass through. Two 3D-printed B<sub>4</sub>C tubes are additionally fitted through the detector holes to further shield internal camera components, as well as to reduce background and light contamination. The full technical specification of the FALCON cameras is given in Table 1.

During measurements, the detectors are mounted on steel plates, which are attached to rails and connected with translation motors, allowing for varying detector distances with respect to the sample position. At the sample position, a rotation stage allows for rotation of the sample over a range of 360°, and thus tomographic measurements can be performed.

For the measurements, the whole system is placed on the sample table of the POLDI instrument [see Fig. 1(b)], which can be translated in *xyz* and rotated for further alignment with respect to the incoming beam. Given that the FALCON detectors are integrating detectors, *i.e.* not having energy discrimination, the chopper and time-of-flight mode of POLDI are not used.

## 2.2. Data acquisition and experimental protocol

The operation of the FALCON cameras and the data acquisition are performed via the image-capture software package *PSL Viewer*, from Photonic Science. Parameters that are mainly modified in between measurements include exposure time per frame, number of frames, frame rate, binning, intensifier gain and output directory. The cameras operate in the quad mode and thus are fully synchronized, and the parameters are set universally. Each camera records a separate image while a combined image from all four cameras (per detector) is created by *PSL Viewer* using a stitching algorithm. In the FALCON system, the individual images from each camera are also corrected for distortion introduced by the lenses and fibre optics, by reference to an individual map file for each camera. These reference map files have been obtained by Photonic Science via measurements with blue light and diffusers. In Section 3, a distortion analysis is performed to verify that the built-in distortion correction is adequate for neutron measurements.

A typical full-scale experiment involves the measurement of samples in tomographic mode, by acquiring a series of diffraction patterns at different sample rotations. Prior to a full tomography, test measurements are taken to tune the scanning parameters to balance data quality versus total measurement time. Initially, the intensifier gain is set at its minimum value and is gradually increased until sufficient diffraction intensities are achieved. While a high intensifier gain can boost low-intensity signals, it does not improve upon the fundamental image quality in terms of better signal-to-noise ratio (SNR) or

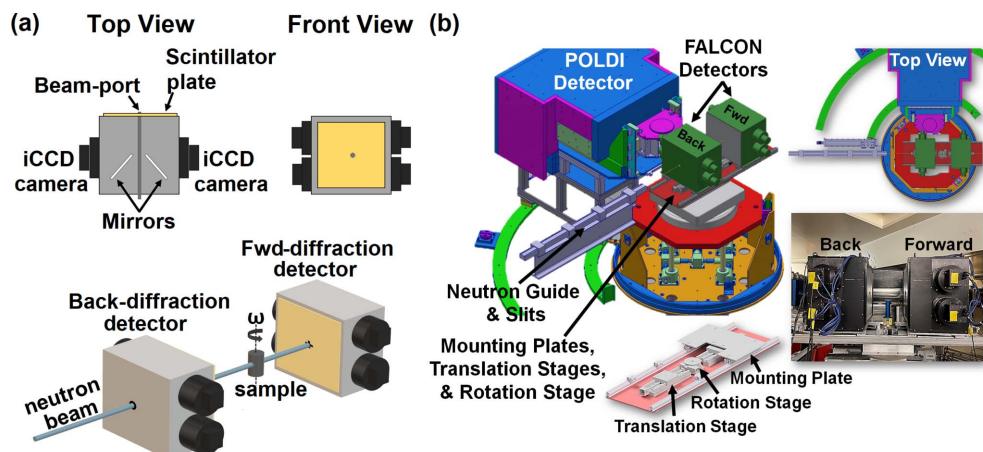


Figure 1

(a) Schematic drawings of the FALCON detectors in top and front view, along with an isoprojection of both detectors highlighting their relative positions with respect to the sample and the incoming neutron beam. (b) A depiction of the FALCON detectors as installed at the POLDI beamline. The detectors are mounted on steel plates connected to translational stages. The whole FALCON mounting system is positioned on the sample table of POLDI.

signal-to-background ratio (SBR) and dynamical range. This can instead be achieved via longer exposure times or binning the diffraction images, with the latter option potentially resulting in lower spatial resolution. Regarding the sample-to-detector distances, one must also consider the sample properties, such as lattice parameters and potential number of grains within the gauge volume. Sample-to-detector distances are chosen to minimize spot overlap while still having sufficient spot resolution on the detector for analysis. Lastly, the total number of projections during a full tomography is considered on the basis of the inherent sample complexity, the intended analysis protocol and the available experimental time.

### 2.3. Data analysis

The main data-analysis procedure includes image preparation, spot indexing and grain mapping, and optional volumetric grain reconstruction. The above processes are presented in detail by Raventós *et al.* (2019), Samothrakitis *et al.* (2020b) and Samothrakitis *et al.* (2022). Here we will thus give only a short overview of each process.

The image cleaning and processing includes (1) median subtraction, (2) outlier removal and filtering, (3) image binarization, and (4) spot labelling. First, the median image of a full tomography dataset is calculated and subtracted from each recorded Laue pattern. This reduces to a high degree background artefacts, such as electronic noise, and the 'skyshine' resulting from the spread of the direct beam at the centre of each detector. Additional noise cleaning is then carried out by applying the removal of outliers and/or Gaussian or median filtering. Next, image binarization is performed by a combination of, for example, the triangle (Zack *et al.*, 1977) or Otsu (Otsu, 1979) binarization method and adaptive thresholding (Bradley & Roth, 2007). Finally, spot labelling of the individual pixels into spots is performed via connected

component analysis of non-zero pixels. This allows us to determine the centre of mass of every individual diffraction spot, later used for the indexing process, as well as its mean intensity and area.

The indexing and overall grain mapping are performed according to the Laue 3DNDT method (Raventós *et al.*, 2019). Laue 3DNDT makes use of a broad continuous neutron wavelength (polychromatic) spectrum and, thus, the recorded diffraction signal is not wavelength resolved and Bragg's equation cannot be directly used to retrieve information. As such, the indexing algorithm was developed according to a forward modelling approach (Schmidt, 2014; Raventós *et al.*, 2019). Given specific experimental parameters (wavelength range, detector size and overall setup) and sample parameters (crystal structure, possible grain positions and orientations), a range of different diffraction patterns are simulated and a library containing the patterns is constructed. Subsequently, every pattern in the library is compared against the experimental diffraction data. A grain is considered indexed once matching conditions between simulations and experiment are found according to well defined fitting-quality criteria. In our algorithm, the orientations are defined as vectors in Rodrigues–Frank formulation (He & Jonas, 2007). An example of a fundamental zone of orientations for a cubic system in Rodrigues–Frank space is given in Fig. 2(c). Once indexing relative to an individual grain has been achieved and the correct (*hkl*) planes have been assigned to the different diffraction spots, further refinement of the grain parameters can be carried out by minimizing the difference between the experimental and calculated scattering vectors (Schmidt, 2014; Oddershede *et al.*, 2010). In this way, the orientation and position resolution for each grain can be optimized. Additionally, experimental parameters, such as detector positions and tilts, as well as exact sample rotation angles ( $\omega$ ) about a vertical axis, are refined through a global fit that includes

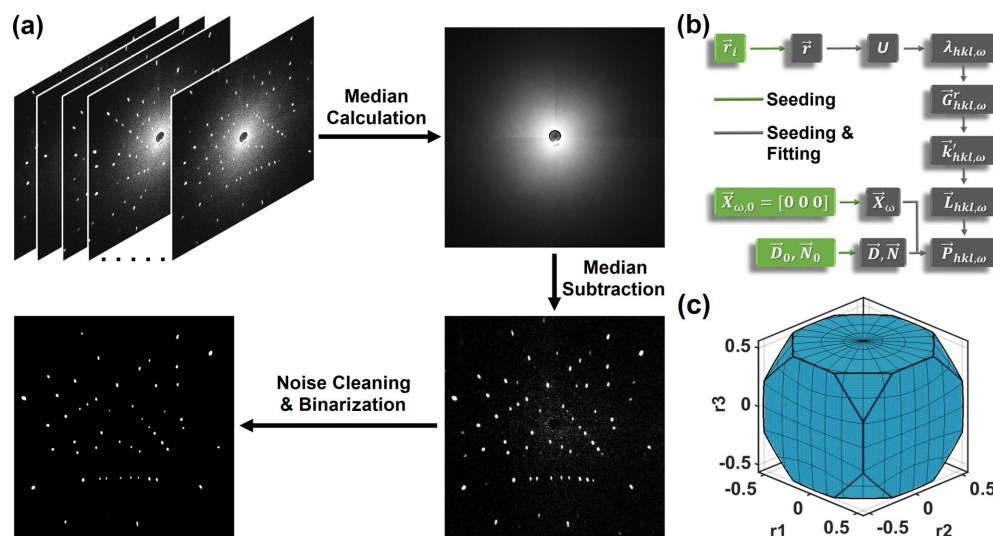


Figure 2

(a) Basic steps of typical image processing including background estimation, background subtraction, noise cleaning and outlier removal, and image binarization and segmentation. (b) A flowchart of the forward model applied for the indexing process. For more detailed information on the definition of symbols, refer to the original work on Laue 3DNDT (Raventós *et al.*, 2019). (c) Fundamental zone of orientations for a cubic crystallographic system in Rodrigues–Frank space.



information from all grains and their associated spots simultaneously.

After indexing, the 3D reconstruction of the grain morphologies can be performed utilizing the *ASTRA* toolbox (van Aarle *et al.*, 2015, 2016) in combination with a 3D vector version of the simultaneous iterative reconstruction technique (Trampert & Leveque, 1990). The orientation and position of the indexed grains along with the shape and intensity of the corresponding reflections are used to create input parameters for the 3D grain morphology reconstruction process (Samothrakitis *et al.*, 2020b).

### 3. Detector characterization measurements: spatial resolution and distortion

Inherent detector effects that are independent of specific beamline properties (*e.g.* the collimation or wavelength spectrum) were characterized. The measurements were performed at the ICON imaging instrument at PSI, Switzerland, owing to its high flux, collimated beam and large field of view (Kaestner *et al.*, 2011). The detectors were installed at the sample table of ICON measurement position 3, offering sufficient space for setup installation. Each of the eight cameras was characterized individually by driving the sample table to consecutively align the centre of each camera with the incoming beam. For the characterization measurements we used a neutron-transparent glass substrate, referred to as the test pattern, onto which a 5  $\mu\text{m}$  Gd layer has been sputtered and laser engraved to form different features with well defined spatial frequencies (Grünzweig *et al.*, 2007; Kaestner *et al.*, 2017). The measurements were performed by taping the test

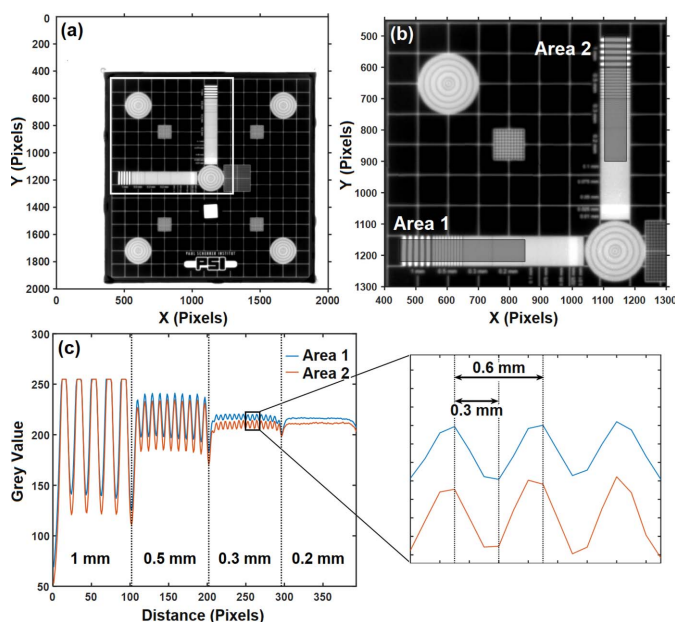


**Figure 3**  
(a) A laser-engraved test pattern, with discrete spatial features, measured on the upper-left camera of the back-scattering detector. (b) A segment of a measurement of the test pattern, including two areas with line spacings ranging from 0.2 to 1.0 mm. (c) The line profiles of areas 1 and 2 as indicated in (b).

pattern directly onto the scintillator plates to ensure minimal distance between them. The recorded images were corrected for dark current and were normalized with open-beam measurements. An example of a corrected image from a single camera is given in Fig. 3(a).

The spatial resolution of the system was assessed in both dimensions by utilizing the regularly spaced line features (area 1 and area 2) of the test pattern, as shown in Fig. 3(b). The corresponding line profiles (lp) in Fig. 3(c) reveal that the system is capable of resolving at least a period of 0.6 mm, *i.e.* a spatial frequency of  $1.667 \text{ lp mm}^{-1}$ . The same result was found for all eight cameras. Overall, the spatial resolution of a scintillator-based detector in conjunction with a CCD camera can be affected by several factors including the thickness of the scintillator and the pixel pitch of the CCD camera. A thicker scintillator increases the detection probability; however, thicker scintillators introduce an increased blur due to the mean path length of secondary particles in the material. Thus, the scintillator needs to be thin enough to not influence the resolution and thick enough to provide high efficiency. The choice of scintillator material is also crucial, as it can affect the interaction probability, light yield and temporal response of the detector.

The distortion analysis was based on the procedure described by Hammersley *et al.* (1994), in which spatial distortions recorded by a 2D detector system are measured using a calibration grid. For our analysis, we make use of the uniformly spaced grid covering the entirety of the test pattern [see Fig. 3(a)], which comprises  $15 \times 15$  squares with

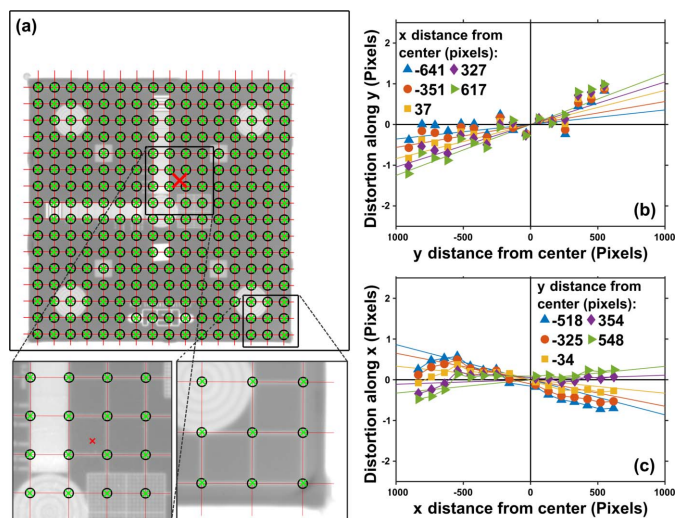


**Figure 4**  
Distortion analysis performed for the upper-right camera of the back-scattering detector, to characterize the geometric distortion effects that remain after the built-in distortion correction from Photonic Science has been applied. (a) The upper-right camera with red lines marking linear fits to the grid lines of the test pattern, black circles denoting the measured line intersections and green crosses denoting the intersection points of the ideal grid pattern. The larger red cross marks the centre of the camera. (b), (c) Distortions defined as the difference between measured and true grid intersection coordinates, plotted for the y and x directions, for selected rows and columns of the grid. The straight lines are linear fits to the data.

**Table 2**

An overview of the measurement parameters for the 6 mm Ø ruby single-crystal sphere, measured at POLDI.

| Measurement No. | Nominal Fwd sample-to-detector distance (mm) | Nominal back sample-to-detector distance (mm) | Exposure time per projection (s) | Total number of projections |
|-----------------|--|---|----------------------------------|-----------------------------|
| 1               | 160  | 160   | 90                               | 91 (0–360°, 4° step)        |
| 2               | 92   | 228   | 35                               | 91 (0–360°, 4° step)        |
| 3               | 92   | 160   | 20                               | 46 (0–360°, 8° step)        |

dimensions of  $1 \times 1$  cm each. Potential distortions were characterized by measuring the  $x$  and  $y$  coordinates of the intersection points of the grid and comparing them with the true dimensions. An example of how these compare for one camera is shown in Fig. 4(a). Close to the camera centre, the measured and actual intersection points overlap almost perfectly, while an increasing difference is observed the closer the intersection points are to the camera edge. This distortion effect is quantified in Figs. 4(b) and 4(c), showing that the distortions in  $x$  and  $y$  are linearly increasing along both the horizontal and vertical directions. Extrapolating this linear trend to the edges of the detectors, one finds a maximum distortion of 0.9 (1) and 1.3 (1) pixels along  $x$  and  $y$ , with a maximum radial distortion of 2.5 (1) pixels. Similar distortion was also found for the remaining seven cameras. Our analysis thus indicates that remnant distortion is negligible and falls well within the resolution limit of the system. In most situations, the above distortion correction should be sufficient. However, a more accurate correction may be beneficial for high-resolution strain fitting and for multi-grain cases where spot densities on the detectors are high.

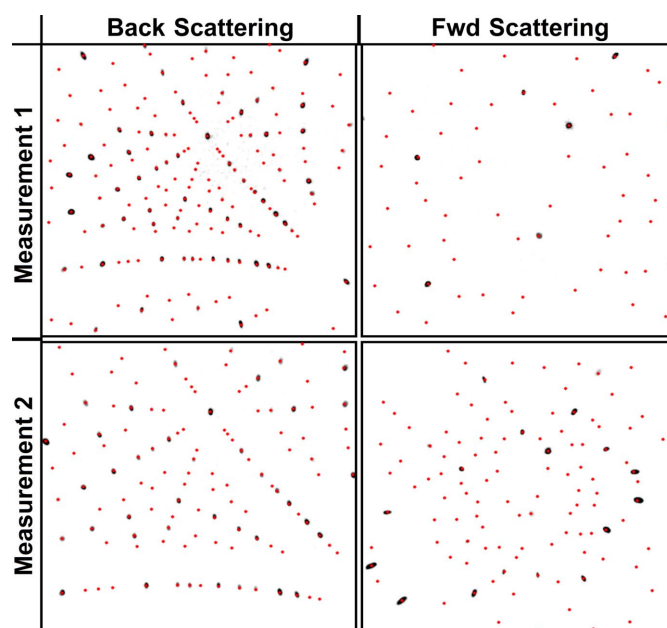
#### 4. Single-crystal measurements

A ruby single-crystal sphere, 6 mm in diameter, was measured to verify detector positions, tilts and offsets, to determine the wavelength range, and to compare the FALCON performance, in terms of SBR and SNR, when used at E11 and POLDI, respectively. First, three consecutive tomographic measurements were performed with different detector positions, number of projections per tomography and exposure times (see Table 2). The three different measurements were performed to check the consistency of our indexing/fitting routine. While the size of the sample is bigger than what is normally used for single-crystal structural studies, leading to difficulties in correcting for extinction effects, it is considered sufficient for calibration measurements. Image processing, indexing and data refinement were performed as described in Section 2.3.

Fig. 5 shows the Laue patterns of the first two measurements, both in back scattering and forward scattering, at the same projection angle. The indexed patterns, indicated by the red markers, are superimposed. From the three measurements, a total of 6864, 5353 and 3042 reflections were recorded, with the majority of the spots assigned to specific ( $hkl$ ) planes. Spots that were not indexed came from the edges of the detectors or were noise/artefacts. Moving the detectors closer to the sample increases the number of viewed ( $hkl$ ) planes and

thus the number of Bragg reflections on each detector. In general, it is important that the sample-to-detector distances are chosen to maximize the information obtained while avoiding overpopulation of the detectors in terms of spot density.

For the indexing of the ruby crystal, we used the lattice parameters  $a = b = 4.7606$  Å and  $c = 12.994$  Å of the  $R\bar{3}c$  space group (Tsirelson *et al.*, 1985). A list of all possible ( $hkl$ ) planes along with the corresponding  $d$  spacing was generated using *Mantid* (Arnold *et al.*, 2014; Mantid, 2013). The refined output parameters of the indexing, along with the minimum and maximum wavelength values calculated, are given in Table 3. The fitting routine and error estimation were carried out following the procedure by Oddershede *et al.* (2010) (see also Section 2.3), wherein the differences between the calculated and experimental scattering vectors in reciprocal space were minimized and the errors were estimated on the basis of a re-scaled covariance matrix. The presented fits were carried out using 5695, 4431 and 2590 diffraction spots for measurements 1, 2 and 3, respectively. Furthermore, extinction effects were estimated by calculating the pixel position difference between recorded and predicted (fitted) spots, from which we found an

**Figure 5**

Back-scattering and forward-scattering Laue diffraction patterns from a 6 mm Ø ruby single-crystal sphere measured at two different detector setups (measurement 1 and measurement 2). The indexed patterns (red markers) are plotted over the recorded patterns. The pixel aspect ratio of the individual images has not been kept 1:1 for plotting purposes.

Table 3

Refined output parameters of the 6 mm  $\varnothing$  ruby single-crystal sphere indexing from the measurements performed at POLDI.

The detector parameters (distances, centres and tilts), as well as the sample position, are given in the laboratory reference system, while the sample orientation is given in the sample reference system. The detector tilts are defined as the rotation angles around the three main axes ( $x$ ,  $y$ ,  $z$ ) of the laboratory reference system. The sample orientations here are given in Euler angles, in the Bunge notation, calculated from the corresponding Rodrigues vectors using the *MTEX* toolbox for MATLAB (Bachmann *et al.*, 2010). For more information on the parameter definitions as well as the different reference systems, refer to Raventós *et al.* (2019).

|   | Measurement 1                           | Measurement 2                             | Measurement 3                             |
|---|---|---|---|
| Fwd-detector distance $x$ (mm)                            | 157.89 (4)                              | 90.00 (3)                                 | 90.96 (4)                                 |
| Fwd-detector centre offset $y$ , $z$ (mm)                 | 0.54 (2)<br>0.96 (2)                    | −1.86 (3)<br>0.55 (3)                     | 0.13 (5)<br>0.07 (5)                      |
| Fwd-detector tilts (radians)                              | 0.0012 (3)<br>−0.0001 (3)<br>0.0016 (3) | 0.0009 (2)<br>−0.0002 (2)<br>−0.0009 (2)  | 0.0019 (4)<br>−0.0019 (3)<br>−0.0027 (3)  |
| Back-detector distance $x$ (mm)                           | −164.80 (2)                             | −233.04 (3)                               | −161.51 (1)                               |
| Back-detector centre offset $y$ , $z$ (mm)                | 0.54 (2)<br>0.96 (2)                    | 1.02 (2)<br>0.71 (3)                      | 0.11 (3)<br>0.08 (3)                      |
| Back-detector tilts (radians)                             | −0.0004 (1)<br>0.0032 (1)<br>0.0000 (2) | −0.0007 (1)<br>0.0021 (2)<br>−0.00009 (2) | −0.0012 (2)<br>−0.0025 (3)<br>−0.0060 (3) |
| Sample orientation $\phi_1$ , $\Phi$ , $\phi_2$ (radians) | 3.7177 (1)<br>0.3929 (1)<br>2.0373 (1)  | 3.7187 (1)<br>0.3927 (1)<br>2.0343 (1)    | 3.7187 (2)<br>0.3926 (1)<br>2.0343 (2)    |
| Sample position $x$ , $y$ , $z$ (mm)                      | 0.15 (2)<br>−0.18 (2)<br>−1.04 (2)      | −0.10 (2)<br>0.01 (2)<br>−1.12 (2)        | 0.21 (3)<br>−0.13 (3)<br>−0.82 (3)        |
| Min. wavelength ( $\text{\AA}$ )                          | 0.5412                                  | 0.7271                                    | 0.5640                                    |
| Max. wavelength ( $\text{\AA}$ )                          | 6.8086                                  | 6.8096                                    | 6.8096                                    |

average difference of 3.6 and 4.1 pixels for the spot position coordinates  $x$  and  $y$ , respectively, on the detectors. Fig. 6 shows a histogram of all wavelengths of the assigned spots, as calculated from the indexing process, plotted in comparison with the measured time-of-flight neutron imaging (Busi *et al.*, 2020) wavelength spectrum of POLDI, showing reasonable resemblance.

To obtain a more comprehensive understanding of the performance of the FALCON detectors at their new location at POLDI, an extra measurement was taken and compared with a corresponding dataset of the same sample collected at E11. The two measurements were performed with the same exposure time and identical detector configuration, including the same gain and binning settings. Both measurements covered a full 360° rotation with 46 projections each (8° step). For the comparison, we located similar projections of the sample in both datasets and identified spots with the same  $hkl$ , and thereby the same structure factor. As such, it was possible to compare the SBR and SNR of the spots as they travel across the detectors. The noise was determined by calculating the standard deviation of the background signal. Figs. 7(a) and 7(b) depict superimposed images recorded over an angular range of 48° for POLDI and 40° for E11. The red boxes and numbers in the figures highlight spots with  $hkl = 102$ , while the insets show zoomed-in views of two such peaks at similar

positions on the detector. In the E11 data, both peak intensities and background levels are generally higher. However, when normalizing the spot intensity to the local background level, the SBR is higher in the POLDI measurements, as shown in Fig. 7(c). This trend is consistent across the measured

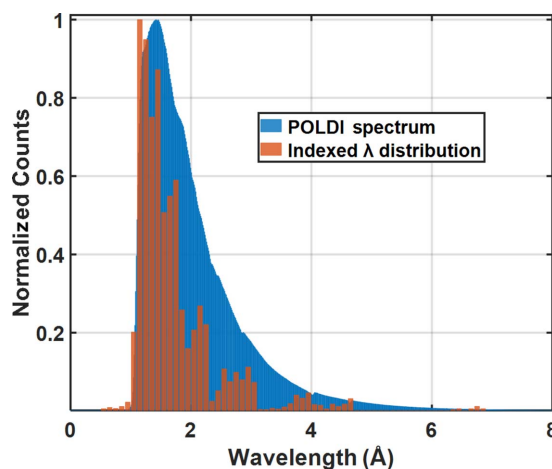


Figure 6

A normalized spectrum of POLDI (blue) with the normalized counts of the indexed wavelengths of the ruby single-crystal measurements superimposed (orange).

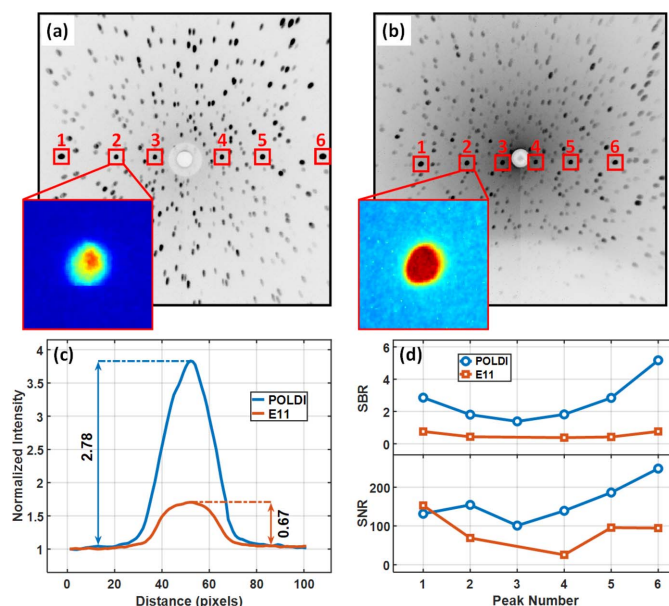


Figure 7

Back-scattering tomography data of a 6 mm  $\varnothing$  ruby single-crystal sphere measured (a) at POLDI, PSI, Switzerland and (b) at E11, HZB, Germany, summed over a range of 48 and 40°, respectively. For comparative analysis, spots with the same  $hkl = 102$  are highlighted and numbered in both datasets, showing how they travel across the detector with rotation. The insets depict examples of two peaks at similar parts of the detector. (c) Average intensity profiles of the peaks given in the insets of (a) and (b). The curves are normalized to their respective backgrounds. (d) The SBR (top) and SNR (bottom) of the  $hkl = 102$  peak. The peak number in the  $x$  axis corresponds to the numbers in (a) and (b). Peak number 3 from the E11 dataset is excluded from the analysis due to saturation. The noise was estimated by calculating the standard deviation of the background signal.



$\omega$  ranges [Fig. 7(d)] and when comparing SNRs for similar spot positions.

Despite the use of identical measurement procedures and detector settings, there are differences in signal quality which can be attributed to factors like neutron flux, background level, beam divergence and wavelength-dependent detector sensitivity. The wavelength spectra of the thermal neutrons used in both cases had a similar range, and the reported neutron fluxes were both of the order of  $\sim 10^8$  neutrons  $\text{s}^{-1} \text{cm}^{-2}$  (Iles & Schorr, 2014; Stühr *et al.*, 2005). Thus, the variations in SBRs and SNRs between the datasets mainly stem from differences in background levels at the detector positions and variations in beam divergences due to differences in beamline collimation configurations.

### 5. Example indexing and grain morphology reconstruction: CoNiGa FSMA

Finally, a comprehensive grain-mapping analysis of a CoNiGa FSMA sample was performed. CoNiGa alloys have garnered attention for their distinctive physical properties, including high magnetic moment, shape-memory effect and susceptibility to significant deformation under a magnetic field (Oikawa *et al.*, 2001, 2006; Dadda *et al.*, 2006). These properties make them promising candidates for various applications such as actuators, sensors and magnetic refrigeration. While CoNiGa single crystals exhibit remarkable stability during cyclical transformation between cubic austenite (B2) and tetragonal martensite ( $\text{L1}_0$ ) (Chernenko *et al.*, 2004), the ductility and toughness of polycrystalline CoNiGa alloys are reduced (Samothrakitis *et al.*, 2020a). This results in premature failure at grain boundaries and intergranular cracking under thermo-mechanical loading, attributed to the high density of grain boundaries and triple points within the samples, as well as the anisotropic volume change displayed by randomly oriented grains. To address this challenge, several processing techniques have been tested to improve the mechanical properties of polycrystalline samples (Vollmer *et al.*, 2015; Lauhoff *et al.*, 2022; Scheibel *et al.*, 2022). Among these techniques, hot extrusion stands out, which involves heating the material above its recrystallization temperature and forcing it through a die to achieve the desired shape (Karsten *et al.*, 2019; Niendorf *et al.*, 2019). This process, combined with meticulous post-extrusion heat treatment, is known to result in grain sizes of the order of millimetres and leads to enhanced ductility by inducing a more uniform oligocrystalline grain structure with reduced defect density, grain boundaries and triple points.

The CoNiGa sample studied here was prepared via hot extrusion followed by post-extrusion heat treatment. After preparation, the sample was cut in half, with one part used for Laue diffraction measurements while the other was characterized by means of EBSD. The sample preparation and EBSD measurement were done as described by Samothrakitis *et al.* (2020a). For the Laue diffraction data collection, the sample was measured at ambient temperature, in tomographic mode, rotated within an angular range of  $360^\circ$  with an angular

step of  $\Delta\omega = 4^\circ$  (91 projections in total). The total scanning time was  $\sim 1.5$  h (60 s per exposure). Similarly to the ruby sample (see Section 4), image processing, indexing and data refinement were performed as described in Section 2.3.

A total number of 17 521 reflections were recorded from all projections and both detectors. The application of the Laue 3DNDT algorithm resulted in the identification of a total of 17 grains within the sample volume, with  $\sim 81\%$  of the detected spots successfully assigned. Visual representations of the recorded detector images are presented in Figs. 8(a) and 8(b), illustrating back and forward scattering at the same projection angle, respectively. Indexed spots corresponding to different grains are superimposed. Spots that are not indexed are attributed to either noise/artefacts, spots originating from grains with low statistics, or spots that were at the very edge of the detectors and thus discarded during the indexing process. Fig. 8(c) provides an isoprojection of the reconstructed 3D model, demonstrating the microstructure of the sample before and after a digital space-filling operation applied to the reconstructed volume. To determine grain size, only the geometry of individual spots for each grain was utilized, disregarding the averaged sum of their intensities. The grains are distinguished by colour according to their orientation, as determined by inverse pole figure (IPF) analysis for a top view of the sample. Notably, the IPF reveals the absence of a discernible preferred crystallographic orientation. To further

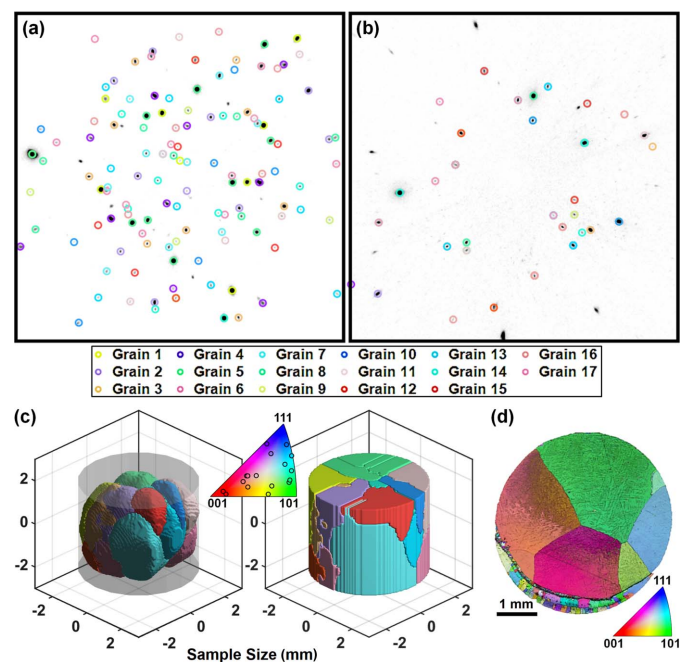


**Figure 8**  
(a), (b) Back-scattering and forward-scattering detector images of the CoNiGa sample. Assigned spots of the 17 indexed grains are superimposed, with the legend colours corresponding to the grain orientations. (c) Three-dimensional grain maps of the sample, as-reconstructed (left) and using a space-filling algorithm (right). For determining the size of the grains, only the geometry of the spots for each grain was used and not their averaged summed intensity. As in (a) and (b), the grains are colour coded according to the IPF in the middle, where the grain orientations are marked for an out-of-plane view (top +z direction). (d) An EBSD IPF map of a cut-off part of the CoNiGa sample, not measured by neutrons.



validate these findings, an IPF map was generated using EBSD measurements performed on the remaining portion of the sample [depicted in Fig. 8(d)]. Consistent with the Laue 3DNDT results, the IPF map from the EBSD corroborates the absence of any significant crystallographic orientation preference. Finally, both the Laue 3DNDT and EBSD analyses indicate that the extrusion process, in conjunction with the subsequent heat treatment, yields coarse millimetre-sized grains.

## 6. Outlook

Within an ongoing project funded by the Swiss Data Science Center, the FALCON capabilities are currently being expanded. The project focuses on developing new robust and scalable algorithms utilizing advanced data-science methods, such as conducting the spot indexing within an optimal transport framework or using machine-learning methods for image processing. The primary objective of this project is to employ an innovative analysis approach to enhance the functionality of the FALCON add-on at POLDI through the new analysis strategy, in an efficient and user-friendly manner.

## 7. Conclusions

In conclusion, this article has described the use of FALCON for Laue 3DNDT experiments at the POLDI beamline of the Paul Scherrer Institute. Standard experimental protocols, data-acquisition strategies and comprehensive characterization measurements of the detector were discussed, including estimation of inherent characteristics such as distortion and resolution.

Initial commissioning measurements with the detector at POLDI were performed on a single crystal. These were used to test and compare the performance between FALCON at E11 and POLDI by comparing signal-to-background and signal-to-noise ratios. Additionally, a full grain map of a CoNiGa oligocrystalline sample demonstrated the performance and feasibility of Laue 3DNDT at POLDI, providing non-destructive resolution of the 3D microstructure of polycrystalline materials using white-beam neutrons with high experimental efficiency.

Accurate characterization of the FALCON performance is crucial for optimal use of the detectors, as well as for future development of the Laue 3DNDT method, particularly for improving morphology reconstruction and strain mapping. Knowledge of the detector performance will allow for more advanced algorithmic developments and ultimately improve the ability to resolve complex 3D microstructures in polycrystalline materials.

Overall, the use of the FALCON double-detector system and the Laue 3DNDT approach present a promising avenue for materials science and condensed matter physics research. With continued advancements in detector technology and algorithmic developments, the potential for non-destructive 3D microstructure resolution will become increasingly accessible to researchers in a variety of fields. With the commis-

sioning of FALCON at POLDI, a forthcoming study will report on new advanced data treatment that will make Laue 3DNDT highly efficient computationally, offering robust and fast results.

## 8. Data availability

The datasets generated and/or analysed during the current study are available from the corresponding author on reasonable request. The Laue 3DNDT code for MATLAB can be found in the GitHub repository ‘Marcraven/Laue3DNDT’, <https://doi.org/10.5281/zenodo.1553164>.

## Acknowledgements

This work was performed at SINQ, Paul Scherrer Institute (PSI), Villigen, Switzerland. The authors wish to thank Dr Denis Cheptikov (PSI), Dr Uwe Filges (PSI) and Dr Michael Tovar (HZB) for their overall contribution.

## Funding information

S. Samothrakitis is supported through a Swiss Data Science Center LSI Track Grant (Project No. C20-14). C. B. Larsen is supported by the Danish National Committee for Research Infrastructure through DanScatt Grant No. 7129-00006B. J. Čapek gratefully acknowledges financial support from the Strategic Focus Area Advanced Manufacturing (SFA-AM) initiative of the ETH Board. J. Kopeček gratefully acknowledges support from the CzechNanoLab Research Infrastructure (LM2023051) and project SOLID21 – CZ.02.1.01/0.0/0.0/16\_019/0000760 supported by MEYS CR.

## References

- Aarle, W. van, Palenstijn, W. J., Cant, J., Janssens, E., Bleichrodt, F., Dabrovolski, A., De Beenhouwer, J., Joost Batenburg, K. & Sijbers, J. (2016). *Opt. Express*, **24**, 25129–25147.
- Aarle, W. van, Palenstijn, W. J., De Beenhouwer, J., Altantzis, T., Bals, S., Batenburg, K. J. & Sijbers, J. (2015). *Ultramicroscopy*, **157**, 35–47.
- Arnold, O., Bilheux, J., Borreguero, J., Buts, A., Campbell, S., Chapon, L., Doucet, M., Draper, N., Ferraz Leal, R., Gigg, M., Lynch, V., Markvardsen, A., Mikkelsen, D., Mikkelsen, R., Miller, R., Palmen, K., Parker, P., Passos, G., Perring, T., Peterson, P., Ren, S., Reuter, M., Savici, A., Taylor, J., Taylor, R., Tolchenov, R., Zhou, W. & Zikovsky, J. (2014). *Nucl. Instrum. Methods Phys. Res. A*, **764**, 156–166.
- Bachmann, F., Hielscher, R. & Schaeben, H. (2010). *Solid State Phenom.* **160**, 63–68.
- Barabash, R. I., Barabash, O. M., Popov, D., Shen, G., Park, C. & Yang, W. (2015). *Acta Mater.* **87**, 344–349.
- Binns, J., McIntyre, G. J. & Parsons, S. (2016). *Acta Cryst.* **B72**, 855–863.
- Bradley, D. & Roth, G. (2007). *J. Graphics Tools*, **12**, 13–21.
- Busi, M., Čapek, J., Polatidis, E., Hovind, J., Boillat, P., Tremis, A. S., Kockelmann, W. & Strobl, M. (2020). *Sci. Rep.* **10**, 14867.
- Cereser, A., Strobl, M., Hall, S. A., Steuwer, A., Kiyanagi, R., Tremis, A. S., Knudsen, E. B., Shinohara, T., Willendrup, P. K., da Silva Fanta, A. B., Iyengar, S., Larsen, P. M., Hanashima, T., Moyoshi, T., Kadletz, P. M., Krooß, P., Niendorf, T., Sales, M., Schmahl, W. W. & Schmidt, S. (2017). *Sci. Rep.* **7**, 9561.
- Chernenko, V., Pons, J., Cesari, E. & Zaslachuk, I. (2004). *Scr. Mater.* **50**, 225–229.

- Cooper, J. B. & Myles, D. A. A. (2000). *Acta Cryst.* **D56**, 246–248.
- Dadda, J., Maier, H., Karaman, I., Karaca, H. & Chumlyakov, Y. I. (2006). *Scr. Mater.* **55**, 663–666.
- Gorbunov, D. I., Henriques, M. S., Qureshi, N., Ouladdiaf, B., Mejía, C. S., Gronemann, J., Andreev, A. V., Petříček, V., Green, E. L. & Wosnitza, J. (2018). *Phys. Rev. Mater.* **2**, 084406.
- Groeber, M. A., Haley, B., Uchic, M. D., Dimiduk, D. M. & Ghosh, S. (2006). *Mater. Charact.* **57**, 259–273.
- Grünzweig, C., Frei, G., Lehmann, E., Kühne, G. & David, C. (2007). *Rev. Sci. Instrum.* **78**, 053708.
- Hammersley, A., Svensson, S. & Thompson, A. (1994). *Nucl. Instrum. Methods Phys. Res. A*, **346**, 312–321.
- He, Y. & Jonas, J. J. (2007). *J. Appl. Cryst.* **40**, 559–569.
- Iles, G. N. & Schorr, S. (2014). *Neutron News*, **25**(2), 27–29.
- Jensen, D. J., Lauridsen, E., Margulies, L., Poulsen, H., Schmidt, S., Sørensen, H. & Vaughan, G. (2006). *Mater. Today*, **9**, 18–25.
- Jensen, D. J. & Poulsen, H. F. (2012). *Mater. Charact.* **72**, 1–7.
- Johnson, G., King, A., Honnicke, M. G., Marrow, J. & Ludwig, W. (2008). *J. Appl. Cryst.* **41**, 310–318.
- Kaestner, A., Kis, Z., Radebe, M., Mannes, D., Hovind, J., Grünzweig, C., Kardjilov, N. & Lehmann, E. (2017). *Phys. Procedia*, **88**, 258–265.
- Karsten, E., Gerstein, G., Golovko, O., Dalinger, A., Lauhoff, C., Krooss, P., Niendorf, T., Samsonenko, A. & Maier, H. (2019). *Shape Mem. Superelasticity*, **5**, 84–94.
- Kolouri, S., Park, S. R., Thorpe, M., Slepcev, D. & Rohde, G. K. (2017). *IEEE Signal Process. Mag.* **34**, 43–59.
- Konijnenberg, P. J., Zaefferer, S. & Raabe, D. (2015). *Acta Mater.* **99**, 402–414.
- Larson, B., Yang, W., Ice, G., Budai, J. & Tischler, J. (2002). *Nature*, **415**, 887–890.
- Lauhoff, C., Pham, T., Paulsen, A., Krooß, P., Frenzel, J., Eggeler, G. & Niendorf, T. (2022). *Metall. Mater. Trans. A*, **53**, 4139–4142.
- Lienert, U., Li, S., Hefferan, C., Lind, J., Suter, R., Bernier, J., Barton, N., Brandes, M., Mills, M., Müller, M., Jakobsen, B. & Pantleon, W. (2011). *JOM*, **63**, 70–77.
- Liu, H., Schmidt, S., Poulsen, H. F., Godfrey, A., Liu, Z., Sharon, J. & Huang, X. (2011). *Science*, **332**, 833–834.
- Ludwig, W., King, A., Reischig, P., Herbig, M., Lauridsen, E. M., Schmidt, S., Proudron, H., Forest, S., Cloetens, P., Roscoat, S. R., Buffière, J. Y., Marrow, T. J. & Poulsen, H. F. (2009a). *Mater. Sci. Eng. A*, **524**, 69–76.
- Ludwig, W., Reischig, P., King, A., Herbig, M., Lauridsen, E., Johnson, G., Marrow, T. & Buffière, J.-Y. (2009b). *Rev. Sci. Instrum.* **80**, 033905.
- Ludwig, W., Schmidt, S., Lauridsen, E. M. & Poulsen, H. F. (2008). *J. Appl. Cryst.* **41**, 302–309.
- Mantid (2013). *Mantid*, <https://www.mantidproject.org/>.
- McDonald, S. A., Reischig, P., Holzner, C., Lauridsen, E. M., Withers, P. J., Merkle, A. P. & Feser, M. (2015). *Sci. Rep.* **5**, 14665.
- Niendorf, T., Lauhoff, C., Karsten, E., Gerstein, G., Liehr, A., Krooß, P. & Maier, H. (2019). *Scr. Mater.* **162**, 127–131.
- Novelli, G., McMonagle, C. J., Kleemiss, F., Probert, M., Puschmann, H., Grabowsky, S., Maynard-Casely, H. E., McIntyre, G. J. & Parsons, S. (2021). *Acta Cryst.* **B77**, 785–800.
- Oddershede, J., Schmidt, S., Poulsen, H. F., Sørensen, H. O., Wright, J. & Reimers, W. (2010). *J. Appl. Cryst.* **43**, 539–549.
- Oikawa, K., Ota, T., Gejima, F., Ohmori, T., Kainuma, R. & Ishida, K. (2001). *Mater. Trans.* **42**, 2472–2475.
- Oikawa, K., Ota, T., Imano, Y., Omori, T., Kainuma, R. & Ishida, K. (2006). *J. Phase Equilibria Diffusion*, **27**, 75–82.
- Otsu, N. (1979). *IEEE Trans. Syst. Man Cybern.* **9**, 62–66.
- Peetermans, S., King, A., Ludwig, W., Reischig, P. & Lehmann, E. (2014). *Analyst*, **139**, 5765–5771.
- Peetermans, S. & Lehmann, E. H. (2013). *J. Appl. Phys.* **114**, 124905.
- Popov, D., Park, C., Kenney-Benson, C. & Shen, G. (2015). *Rev. Sci. Instrum.* **86**, 072204.
- Poulsen, H. F., Nielsen, S. F., Lauridsen, E. M., Schmidt, S., Suter, R. M., Lienert, U., Margulies, L., Lorentzen, T. & Juul Jensen, D. (2001). *J. Appl. Cryst.* **34**, 751–756.
- Purushottam Raj Purohit, R. R. P., Tardif, S., Castelnau, O., Eymery, J., Guinebreière, R., Robach, O., Ors, T. & Micha, J.-S. (2022). *J. Appl. Cryst.* **55**, 737–750.
- Raventós, M., Tovar, M., Medarde, M., Shang, T., Strobl, M., Samothrakitis, S., Pomjakushina, E., Grünzweig, C. & Schmidt, S. (2019). *Sci. Rep.* **9**, 4798.
- Samothrakitis, S., Larsen, C. B., Čapek, J., Polatidis, E., Raventós, M., Tovar, M., Schmidt, S. & Strobl, M. (2022). *Mater. Today Adv.* **15**, 100258.
- Samothrakitis, S., Larsen, C. B., Woracek, R., Heller, L., Kopeček, J., Gerstein, G., Maier, H. J., Rameš, M., Tovar, M., Šittner, P., Schmidt, S. & Strobl, M. (2020a). *Mater. Des.* **196**, 109118.
- Samothrakitis, S., Raventós, M., Čapek, J., Larsen, C. B., Grünzweig, C., Tovar, M., García-González, M., Kopeček, J., Schmidt, S. & Strobl, M. (2020b). *Sci. Rep.* **10**, 3724.
- Sato, H., Shiota, Y., Morooka, S., Todaka, Y., Adachi, N., Sadamatsu, S., Oikawa, K., Harada, M., Zhang, S., Su, Y., Kamiyama, T., Ohnuma, M., Furusaka, M., Shinohara, T. & Kiyana, Y. (2017). *J. Appl. Cryst.* **50**, 1601–1610.
- Scheibel, F., Lauhoff, C., Riegg, S., Krooß, P., Bruder, E., Adabifiroozjaei, E., Molina-Luna, L., Böhm, S., Chumlyakov, Y. I., Niendorf, T. & Gutfleisch, O. (2022). *Adv. Eng. Mater.* **24**, 2200069.
- Schmidt, S. (2014). *J. Appl. Cryst.* **47**, 276–284.
- Smeets, S., Zou, X. & Wan, W. (2018). *J. Appl. Cryst.* **51**, 1262–1273.
- Stechmann, G., Zaefferer, S., Konijnenberg, P., Raabe, D., Gretener, C., Kranz, L., Perrenoud, J., Buecheler, S. & Tiwari, A. N. (2016). *Solar Energy Mater. Solar Cells*, **151**, 66–80.
- Stuhr, U., Grosse, M. & Wagner, W. (2006). *Mater. Sci. Eng. A*, **437**, 134–138.
- Stuhr, U., Spitzer, H., Egger, J., Hofer, A., Rasmussen, P., Graf, D., Bollhalder, A., Schild, M., Bauer, G. & Wagner, W. (2005). *Nucl. Instrum. Methods Phys. Res. A*, **545**, 330–338.
- Trampert, J. & Leveque, J.-J. (1990). *J. Geophys. Res.* **95**, 12553–12559.
- Tsirelson, V. Yu., Antipin, M., Gerr, R., Ozerov, R. & Struchkov, Y. T. (1985). *Phys. Status Solidi A*, **87**, 425–433.
- Vollmer, M., Krooß, P., Segel, C., Weidner, A., Paulsen, A., Frenzel, J., Schaper, M., Eggeler, G., Maier, H. J. & Niendorf, T. (2015). *J. Alloys Compd.* **633**, 288–295.
- Woracek, R., Penumadu, D., Kardjilov, N., Hilger, A., Boin, M., Banhart, J. & Manke, I. (2014). *Adv. Mater.* **26**, 4069–4073.
- Woracek, R., Santisteban, J., Fedrigo, A. & Strobl, M. (2018). *Nucl. Instrum. Methods Phys. Res. A*, **878**, 141–158.
- Zack, G. W., Rogers, W. E. & Latt, S. A. (1977). *J. Histochem. Cytochem.* **25**, 741–753.
- Zaefferer, S., Wright, S. & Raabe, D. (2008). *Metall. Mater. Trans. A*, **39**, 374–389.
- Zerdane, S., Mariette, C., McIntyre, G. J., Lemée-Cailleau, M.-H., Rabiller, P., Guérin, L., Ameline, J. C. & Toudic, B. (2015). *Acta Cryst.* **B71**, 293–299.
- Zhu, W., Wu, G., Godfrey, A., Schmidt, S., He, Q., Feng, Z., Huang, T., Zhang, L. & Huang, X. (2022). *Scr. Mater.* **214**, 114677.